PHYSICAL REVIEW B VOLUME 58, NUMBER 3 15 JULY 1998-I

Surface response of a fluid-loaded solid to impulsive line and point forces: Application to scanning acoustic microscopy

A. G. Every
Department of Physics, University of the Witwatersrand, PO WITS 2050, South Africa

G. A. D. Briggs
Department of Materials, Oxford University, Oxford OX1 3PH, United Kingdom

(Received 8 September 1997)

Algorithms are presented for calculating the two- and three-dimensional time domain dynamic Green's functions of a pair of joined semi-infinite anisotropic elastic continua. They are used to calculate the normal surface displacement response of fluid-loaded solids to impulsive line and point forces. Particular attention is given to the resonant and singular features in the response associated with the Stoneley-Scholte interfacial wave, leaky Rayleigh and pseudosurface acoustic waves, and lateral waves, i.e., surface skimming bulk waves of the solid and of the liquid. The various regimes are explored, in which the fluid sound speed and acoustic impedance range from small to large as compared to those of the solid. The effects of elastic anisotropy of the solid are illustrated with results for a carbon fiber composite and for the principal crystallographic cuts of a number of cubic crystals of anisotropy coefficient $\eta = 2C_{44}/(C_{11} - C_{12})$ greater and less than unity. Calculated images, representing the dependence of the normal displacement response on time and direction, are in good agreement with published acoustic microscopy images of a number of anisotropic solids that have been measured with a configuration of two line focus or two point focus lenses. These images display prominent features due to leaky Rayleigh and pseudosurface waves, as well as sharper lateral wave structures. The mode of excitation and detection does not, however, couple into the water lateral wave and Sholte wave, which are absent from the measured images. This effect is simulated by setting a finite cutoff, determined by the aperture angles of the lenses, to the spatial Fourier transform of the surface Green's function. [S0163-1829(98)06327-9]

I. INTRODUCTION

The dynamics of the fluid-solid interface is a subject that cuts across many fields, including materials characterization and nondestructive testing, condensed matter physics, physical and ocean acoustics, continuum mechanisms, and seismology. There is extensive literature on the subject, going back more than a century, and it is given prominent coverage in numerous books (see, e.g., Refs. 1–4). A multitude of different physical phenomena have been investigated, including the reflection and transmission of plane waves, reflection of bounded beams and the Schoch wave phenomenon,[5] Rayleigh surface waves and their attenuation through leakage of energy into the fluid,[6] transient waves and waves generated by line and point sources,[7] and attendant effects including the Stoneley-Scholte interfacial wave,[8–11] head waves and lateral waves,[12] the vibration of fluid loaded plates,[13] and the influence of prestress[14] and viscoelasticity on Scholte waves.[15]

The dynamics of the liquid-solid interface play a central role in acoustic microscopy, in the interpretation of both frequency and time domain phenomena.[16] Recently, an application has been found for the surface dynamical response functions of liquid-loaded anisotropic solids[17] in the interpretation of a series of experiments conducted by Vines and co-workers,[18–22] in which they use a configuration of two line focus or two point focus acoustic lenses to study the surface dynamics of crystals and other anisotropic solids. By rotating the solid about its surface normal, they obtain information pertaining to wave propagation in different directions along the liquid loaded surface or, more to the point as we argue in this paper, the dynamic response to impulsive line or point forces acting normally on the water-loaded surface. Their technique complements conventional acoustic microscopy using a single line focus lens, which has proved to be of great value in the study of the surface dynamics of anisotropic solids.

The measurements of Vines and co-workers using line focus lenses reveal information about the two-dimensional response of a surface since coherent excitation and detection take place along parallel lines in the surface, in the direction of which there is translational invariance. This fixes the direction of the $\mathbf{k}_\parallel$'s that can be excited. Hsu *et al.*[23] and Li and Achenbach[24] have carried out time-resolved measurements with a single line focus lens in negative defocus and the results they obtain, apart from the specularly reflected axial wave, are similar to the line focus measurements of Vines and co-workers. This is to be expected, since in effect there are two physically separated regions on opposite sides of the lens axis, where excitation and sensing takes place.

The measurements of Vines and co-workers with point focus lenses, by contrast, probe the three-dimensional dynamic response of the surface. Acoustic microscopy employing a single point focus lens has also been used to study anisotropic solids, but the physical interpretation of the results is complicated by the fact that propagation in many directions in the surface is folded into the recorded signal[25] and beating effects can arise from interference between surface and pseudosurface wave contributions.[26]

The acoustic microscopy techniques of Vines and co-workers[18–20] and Hsu *et al.*[23] provide useful approaches to the surface characterization of anisotropic materials. Obvious areas of application are the determination of (constant or spatially varying) near surface elastic constants and the detection of surface flaws. The realization of this potential is, however, contingent on the availability of satisfactory methods for calculating the signals. Hsu *et al.*[23] have reported that a Green's function method is able to account for their line focus measurements and Li and Achenbach[24] have used a reflection function analysis to obtain the elastic constants of anisotropic solids from time resolved measurements with a single line focus lens. As regards the point focus images of Vines and co-workers,[18,19,22] only a partial account was provided by the originators of this technique in terms of surface wave group velocity curves.[19,21] In a recent paper, Every, Maznev, and Briggs[17] have pointed out that a Green's function approach is able to provide a fuller account of these measured images.

In this paper we argue that in the pulsed mode experiments of Vines and co-workers,[18–20] the line or point focus source transducer gives rise to a concentrated line or point force of short duration normal to the surface of the solid and by reciprocity the receiver transducer measures the normal displacement at its focal line/point elsewhere on the surface at a later time t. The measured signal might therefore be expected to mimic the two- and three-dimensional (2D/3D) elastodynamic Green's functions $G_{33}(\mathbf{x}_\parallel, t)$ for the fluid loaded surface of the solid [the subscripts of $\mathbf{G}$ refer to normal force and displacement in the x_3 direction, while $\mathbf{x}_\parallel = (x_1, x_2)$ is the position vector in the surface of the sensing point relative to the excitation point]. Our calculated Green's functions, represented as images spanning time and direction in the surface, conform well to measurement. Because of the finite aperture angle θ of the two lenses, the spatial Fourier transforms of the forcing and sensing areas have a finite cutoff at a slowness $s = k/\omega = v^{-1}\sin\theta$, where $v \approx 1500$ m/s is the speed of sound in water, and only modes with surface slownesses less than this are excited and observed with this technique. There are other methods of excitation (laser thermoacoustic, laser induced vaporization,[9] the use of interdigital transducers[10] and capillary fracture, etc.) and detection (optical interferometry or beam deflection, contact capacitive or piezoelectric transducers, etc.) that in principal permit or in some cases have already led to the observation of the Scholte interfacial wave whose slowness exceeds v^{-1}. Our calculations without cutoff are applicable in this case.

The solids that are studied by means of acoustic microscopy and related techniques vary widely in their acoustic properties, as do the coupling liquids that can be employed. While many solids have sound velocities and acoustic impedances significantly greater than the coupling liquid (most commonly it is water that is used), there are some combinations that are comparable in velocity and acoustic impedance (e.g., carbon fiber epoxy composites and water) and some combinations in which one or more of the solids velocities is less than that of the liquid (e.g., polyethylene or polystyrene and water). Many of the materials that are studied are elastically anisotropic. The consequence of this is that there is a wealth of different types of behavior to be observed. One aim of this paper is to explore, through a broad range of examples, the different regimes of behavior possible within the parameter space defined by the relative velocities and acoustic impedances of the solid and coupling fluid and also to point out some of the consequences of elastic anisotropy of the solid. We accomplish the latter by presenting gray-scale images for a number of materials and crystallographic orientations, in which the axes span time and direction in the surface and the displacement response is represented by the brightness. In many cases the examples are chosen for comparison with published experimental images.

II. METHOD OF CALCULATION

We describe here algorithms for calculating the time domain displacement response of two joined linear elastically anisotropic halfspaces to impulsive line and point forces acting at their interface. These algorithms are generalizations of methods for calculating the response functions of a single anisotropic halfspace that have been reported elsewhere.[27,28] They are adapted for application to the water-loaded solid surface by the simple expedient of taking the second medium to be isotropic and letting its shear modulus tend to zero. Liquid viscosity and solid viscoelasticity is not considered.

We consider a general anisotropic elastic continuum of density ρ^+ and elastic modulus tensor C^+_{ijkl} occupying the half space $x_3 > 0$ and joined to a second continuum of density ρ^- and elastic modulus C^-_{ijkl} occupying the half space $x_3 < 0$. The time-dependent displacement response to an impulsive line force acting along the x_2 axis and to a point force acting at the origin are treated respectively in the next two subsections.

A. Line force response

A concentrated impulsive line force $\mathbf{F}$ per unit length acts along the x_2 axis in the interface between the two half spaces. The time-dependent displacement field in response to this force

$$u_i(\mathbf{x}, t) = G_{ij}(\mathbf{x}, t) F_j, \tag{1}$$

where $G_{ij}(\mathbf{x}, t)$ is the 2D dynamic Green's function, is governed by the the equations of motion[1]

$$\rho^{\pm} \frac{\partial^2 u_i}{\partial t^2} = C^{\pm}_{ijkl} \frac{\partial^2 u_l}{\partial x_j \partial x_k}, \quad x_3 \neq 0, \tag{2}$$

in each of the media and is subject to the boundary conditions on the stress tensor

$$\sigma_{\ell 3}(\mathbf{x}_\parallel, x_3 = 0_+, t) - \sigma_{\ell 3}(\mathbf{x}_\parallel, x_3 = 0_-, t) = -F_j \delta_{j\ell} \delta(x_1) \delta(t), \tag{3}$$

which express the requirement that the traction forces must balance the applied force. Representing the boundary conditions in terms of their Fourier transform $F_j \delta_{j\ell} \mathcal{F}(\mathbf{k}_\parallel, \omega)$,

$$\mathcal{F}(\mathbf{k}_\parallel, \omega) = -\delta(k_2)/4\pi^2, \tag{4}$$

with respect to $\mathbf{x}_\parallel$ and t, we have that

$$\sigma_{\ell 3}(\mathbf{x}_\parallel ,x_3=0_+ ,t)-\sigma_{\ell 3}(\mathbf{x}_\parallel ,x_3=0_- ,t) = \int_{-\infty}^{\infty} d^2k_\parallel \int_{-\infty}^{\infty} d\omega \; F_j \delta_{j\ell}\mathcal{F}(\mathbf{k}_\parallel ,\omega) \times \exp\{i\mathbf{k}_\parallel\cdot\mathbf{x}_\parallel-\omega t\}, \tag{5}$$

where $\mathbf{k}_\parallel=(k_1,k_2)$ is the projection of the wave vector $\mathbf{k}$ in the surface and ω is the angular frequency. We seek a solution to the equations of motion (2) and boundary conditions (5), which in each medium takes the form of a superposition of outgoing plane waves whose amplitudes are proportional to F_j:

$$u_i(\mathbf{x},t)=\int_{-\infty}^{\infty} d^2k_\parallel \int_{-\infty}^{\infty} d\omega \sum_n A_j^{(n)} F_j U_i^{(n)} \times \exp\{i(\mathbf{k}_\parallel\cdot\mathbf{x}_\parallel+k_3^{(n)}x_3-\omega t)\}, \tag{6}$$

n running from 1 to 3 for the upper half space and from 4 to 6 for the lower. For each value of $\mathbf{k}_\parallel$ and ω, the third component k_3 of $\mathbf{k}$ and the polarization vector $\mathbf{U}$ are related through the Christoffel equations[1]

$$(C_{ijkl}^{\pm}s_j s_k-\rho^{\pm}\delta_{il})U_l=0 \tag{7}$$

for each medium, where $\mathbf{s}=\mathbf{k}/\omega$ is the acoustic slowness vector. The sextic characteristic equation

$$\det|C_{ijkl}^{\pm}s_j s_k-\rho^{\pm}\delta_{il}|=0, \tag{8}$$

yields six solutions for s_3 for each medium, from which three are chosen that correspond to outgoing waves, on the basis that they are either homogeneous (bulk) waves with ray vectors pointing away from the interface or inhomogeneous (evanescent) waves that decay away from the interface.

From the stress-strain relationship $\sigma_{lm}=C_{lmpq}\partial u_p/\partial x_q$ and Eq. (6) it follows that the surface tractions are given by

$$\sigma_{\ell 3}(\mathbf{x}_\parallel ,x_3=0_\pm ,t) = \int_{-\infty}^{\infty} d^2k_\parallel \int_{-\infty}^{\infty} d\omega \; i\omega \sum_n A_j^{(n)} F_j B_\ell^{(n)} \times \exp\{i(\mathbf{k}_\parallel\cdot\mathbf{x}_\parallel-\omega t)\}, \tag{9}$$

where

$$B_\ell^{(n)}=\pm\sum_{p,q} C_{3\ell pq}U_p^{(n)}s_q^{(n)}, \tag{10}$$

with + ($n=1,2,3$) and − ($n=4,5,6$) pertaining to the upper and lower half spaces, respectively. Comparing Eqs. (5) and (9), we arrive at a set of three linear equations for the partial wave weighting factors $A_j^{(n)}$,

$$\sum_{n=1}^{6} A_j^{(n)}B_l^{(n)}=\delta_{jl}\mathcal{F}(\mathbf{k}_\parallel ,\omega)/i\omega, \quad l=1,2,3. \tag{11}$$

Another three equations for the weighting factors are obtained from continuity of the displacement field at the interface,

$$\sum_{n=1}^{6} A_j^{(n)}B_l^{(n)}=0, \quad l=4,5,6, \tag{12}$$

where $B_l^{(n)}$ equals $U_{l-3}^{(n)}$ for the upper half space and $-U_{l-3}^{(n)}$ for the lower. These six linear equations have the solution

$$A_j^{(n)}=\frac{1}{i\omega}\,\mathcal{F}(\mathbf{k}_\parallel ,\omega)(\mathbf{B}^{-1})_j^{(n)}. \tag{13}$$

From Eqs. (1), (6), and (13) it follows that

$$G_{ij}(\mathbf{x},t)=\int_{-\infty}^{\infty} d^2k_\parallel \int_{-\infty}^{\infty} \frac{d\omega}{i\omega}\,\mathcal{F}(\mathbf{k}_\parallel ,\omega)\sum_n (\mathbf{B}^{-1})_j^{(n)}U_i^{(n)} \times \exp\{i(\mathbf{k}_\parallel\cdot\mathbf{x}_\parallel+k_3^{(n)}x_3-\omega t)\}. \tag{14}$$

Regarding the response at the interface, we can without loss of generality take the observation point $\mathbf{x}_\parallel$ to be in the positive direction along the x_1 axis in the surface, setting $x_1=x_3=0$. On substituting for $\mathcal{F}(\mathbf{k}_\parallel ,\omega)$ from Eq. (4) into Eq. (14), replacing the integration variable $\mathbf{k}_\parallel$ by $\mathbf{s}_\parallel=\mathbf{k}_\parallel/\omega$, and integrating with respect to s_2, we obtain

$$G_{ij}(x_1,t)=\int_{-\infty}^{\infty} ds_1 \int_{-\infty}^{\infty} d\omega \, \frac{i\Psi(s_1,s_2=0)}{4\pi^2} \times \exp\{i\omega(s_1x_1-t)\}, \tag{15}$$

where

$$\Psi_{ij}(s_1,s_2)=\sum_{n=1}^{3}(\mathbf{B}^{-1})_j^{(n)}U_i^{(n)}=\sum_{n=1}^{3}\frac{\mathrm{adj}(\mathbf{B})_j^{(n)}U_i^{(n)}}{\det|\mathbf{B}|}, \tag{16}$$

adj denoting the adjoint matrix. $\Psi_{ij}(s_1,s_2)$, which we will call the surface admittance function, plays a key role in the subsequent analysis.

Since $G_{ij}(x_2,t)$ is real, it follows that its temporal Fourier transform has the property $\tilde{G}_{ij}^{*}(x_1,\omega)=\tilde{G}_{ij}(x_1,-\omega)$, where the asterisk denotes complex conjugation. We exploit this property to restrict the integration over ω in Eq. (15) to the interval $[0,\infty]$, retaining only the real part. On carrying out the integration, making the replacement $(s_1x_1-t)\rightarrow(s_1x_1-t+i0_+)$ for convergence, we arrive at the result

$$G_{ij}(x_1,t)=-\frac{1}{2\pi^2}\left[\frac{1}{x_1}\,\mathrm{P}\int_{-\infty}^{+\infty} ds_1\,\frac{\mathrm{Re}\,\Psi_{ij}(s_1,0)}{(s_1-t/x_1)} + \frac{\pi}{|x_1|}\,\mathrm{Im}\,\Psi_{ij}(t/x_1,0)\right], \tag{17}$$

with $\mathrm{P}\int$ denoting the principal value of the integral.

From causality, the displacement is zero for negative times. Using this fact and setting $G_{ij}(-x_1,-t)=0$, $t>0$, in Eq. (17) yields the Kramers-Kronig–type relation

$$\frac{1}{x_1}\,\mathrm{P}\int_{-\infty}^{+\infty} ds_1\,\frac{\mathrm{Re}\,\Psi_{ij}(s_1,0)}{(s_1-t/x_1)}=\frac{\pi}{|x_1|}\,\mathrm{Im}\,\Psi_{ij}(t/x_1,0), \quad t>0. \tag{18}$$

It follows from Eq. (17) that

$$G_{ij}(x_1,t>0)=-\frac{1}{\pi|x_1|}\,\mathrm{Im}\,\Psi_{ij}(t/x_1,0), \tag{19}$$

which has reduced the calculation of the line force response to a purely algebraic problem.

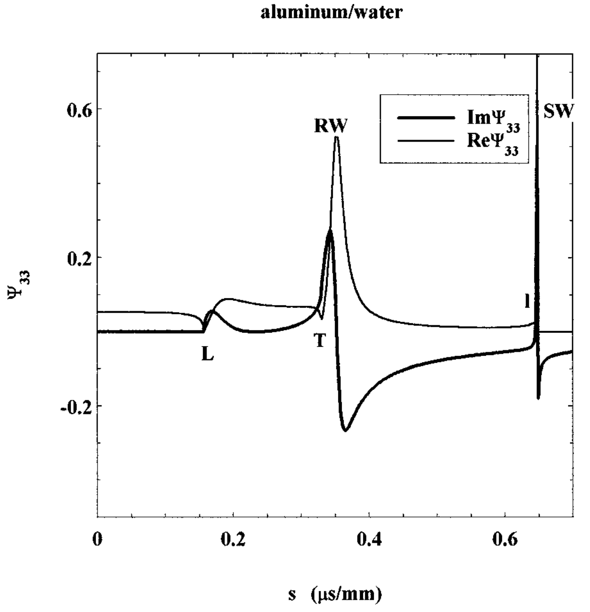

FIG. 1. Ψ_{33} for the water-loaded aluminum surface.

Figure 1 shows the admittance function Ψ_{33} for the combination isotropic polycrystalline aluminium and water. Apart from a factor $-1/\pi|x_1|$, $\mathrm{Im}\,\Psi_{33}$ is the normal displacement response of the surface to an impulsive line force, expressed as a function of t/x_1. It is zero until the longitudinal wave arrival or lateral wave of the solid, labeled L, because in this fully supersonic region all the solutions of Eq. (8) are real and hence Ψ_{33} is pure real. $\mathrm{Re}\,\Psi_{33}$ has a sharp minimum at L. At the transverse lateral wave of the solid, labeled T, $\mathrm{Im}\,\Psi_{33}$ displays a kink, while $\mathrm{Re}\,\Psi_{33}$ has another sharp minimum. The broadened resonance feature, labeled RW, is the leaky Rayleigh wave of the solid, which is dampened through radiation of energy into the liquid. Beyond RW, $\mathrm{Re}\,\Psi_{33}$ falls off rapidly to a very small value, but towards the water slowness $s_{\ell}=1/v(\mathrm{water})=0.645\ \mu\mathrm{s/mm}$ it increases again and then drops to zero at s_{ℓ} to form the lateral wave feature labeled l. Beyond s_{ℓ}, Ψ_{33} is pure imaginary, except at $s_{\mathrm{SW}}=0.6475\ \mu\mathrm{s/mm}$, where $\mathrm{Re}\,\Psi_{33}$ displays a δ-function singularity associated with the Scholte wave (SW) pole, which is conditioned on the vanishing of the boundary condition determinant $\det|\mathbf{B}|$. This is a true interfacial wave that falls off exponentially with distance on both sides of the interface. It is a special case of the Stoneley wave,[29] but the conditions on its existence are less exclusive than for Stoneley waves at the interface between joined solids.[30] To render this singularity visible it has been artificially broadened by making the replacement

$$\Psi_{33}\rightarrow 1/(1/\Psi_{33}+\alpha), \tag{20}$$

where α is a small but finite positive number. $\mathrm{Im}\,\Psi_{33}$, and hence the line force response, also displays corresponding resonant or singular features at RW, l, and SW.

A global picture of Ψ_{33} for an anisotropic surface is provided by Fig. 2, which shows $\mathrm{Re}\,\Psi_{33}(\mathbf{s}_{\parallel})$ for the water-loaded (001) surface of copper as a gray-scale image. The lines that stand out as darker are the longitudinal (L) and transverse (T) lateral waves of the solid and correspond to loci of the projection on the surface of limiting or threshold bulk wave slownesses of the solid, whose ray vectors are parallel to the (001) plane. Solutions of Eq. (8) change from real to complex on these lines. The very bright bands that appear to repel at about 30° and 60° to [100] correspond to the leaky RW near the ⟨100⟩ directions and leaky pseudosurface acoustic wave (PSAW) near the ⟨110⟩ directions. The RW trace lies outside the bulk slowness threshold curve for the slow transverse (ST) branch (the so-called transonic state for the solid), except in the ⟨110⟩ directions, where it degenerates with the limiting bulk slowness. In the ⟨100⟩ directions the RW is pure SV (shear vertical, i.e., polarized in the sagittal plane), whereas towards the ⟨110⟩ directions its polarization tilts over to SH (shear horizontally polarized). As it does so, the coupling to the water and consequent damping decrease and the RW becomes sharper but less intense. The PSAW, on the other hand, is SV in the ⟨110⟩ directions, and moving away from these directions its polarization tilts over and it fades in intensity. Beyond the RW, $\mathrm{Re}\,\Psi_{33}(\mathbf{s}_{\parallel})$ falls off in value, but near $|\mathbf{s}_{\parallel}|=1/v(\mathrm{water})$, it increases again, drops to zero at the lateral wave l, and then displays a singular spike associated with the Scholte wave SW at the interface. The l and SW features are too close to be resolved in this diagram and their jagged appearance is an artifact of the finite resolution of this image.

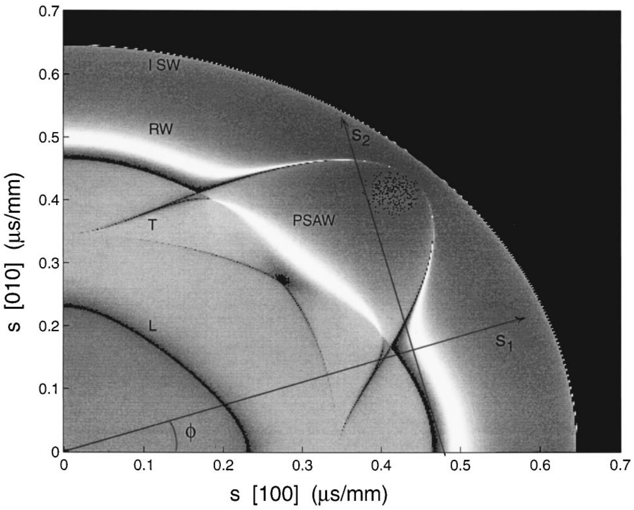

FIG. 2. Representation of $\mathrm{Re}\,\Psi_{33}(\mathbf{s}_{\parallel})$ as a gray-scale image for the water-loaded (001) surface of copper. The pattern repeats itself in the other three quadrants. The integration path in the calculation of the point force response is along the line s_2.

B. Point force response

For an impulsive point force, it is expedient to obtain the 3D dynamic Green's function $G_{ij}(\mathbf{x},t)=(\partial/\partial t)H_{ij}(\mathbf{x},t)$ as the time derivative of the displacement response $H_{ij}(\mathbf{x},t)$ to a concentrated point force acting at the origin and having unit step function time dependence. The boundary conditions obtaining for the calculation of H_{ij} are

$$\sigma_{\ell 3}(\mathbf{x}_{\parallel},x_3=0_+,t)-\sigma_{\ell 3}(\mathbf{x}_{\parallel},x_3=0_-,t)$$
$$=-F_j\delta_{j\ell}\delta(x_1)\delta(x_2)\epsilon(t), \tag{21}$$

with

$$\boldsymbol{\epsilon}(t)=\begin{cases} \frac{1}{2}, & t>0 \\ -\frac{1}{2}, & t<0. \end{cases} \tag{22}$$

Their Fourier transform is $F_j\delta_{j\ell}\mathcal{F}(\mathbf{k}_\parallel,\omega)$,

$$\mathcal{F}(\mathbf{k}_\parallel,\omega)=1/8\pi^3 i\omega. \tag{23}$$

In place of Eq. (14), $G_{ij}(\mathbf{x},t)$ is in this case given by

$$G_{ij}(\mathbf{x},t)=\frac{\partial}{\partial t}\int_{-\infty}^{\infty}d^2k_\parallel\int_{-\infty}^{\infty}\frac{d\omega}{i\omega}\,\mathcal{F}(\mathbf{k}_\parallel,\omega)\sum_n(\mathbf{B}^{-1})_j^{(n)}U_i^{(n)}$$
$$\times\exp\{i(\mathbf{k}_\parallel\cdot\mathbf{x}_\parallel+k_3^{(n)}x_3-\omega t)\}. \tag{24}$$

Regarding the response at the interface, we again set $x_1=x_3=0$. On substituting for $\mathcal{F}(\mathbf{k}_\parallel,\omega)$ in Eq. (24) and replacing the integration variable $\mathbf{k}_\parallel$ by $\mathbf{s}_\parallel=\mathbf{k}_\parallel/\omega$, we obtain

$$G_{ij}(x_1,t)=-\frac{\partial}{\partial t}\int_{-\infty}^{\infty}ds_1\int_{-\infty}^{\infty}d\omega\,\frac{\Phi_{ij}(s_1)}{8\pi^3}$$
$$\times\exp\{i\omega(s_1x_1-t)\}, \tag{25}$$

where

$$\Phi_{ij}(s_1)=\int_{-\infty}^{\infty}ds_2\Psi_{ij}(s_1,s_2). \tag{26}$$

As before, we restrict the integration over ω in Eq. (25) to the interval $[0,\infty]$, retaining only the real part. On carrying out this integration we obtain

$$G_{ij}(x_1,t)=-\frac{\partial}{\partial t}\frac{1}{4\pi^3}\left[-\frac{1}{x_1}\,\mathrm{P}\int_{-\infty}^{+\infty}ds_1\,\frac{\mathrm{Im}\,\Phi_{ij}(s_1)}{(s_1-t/x_1)}\right.$$
$$\left.+\frac{\pi}{|x_1|}\,\mathrm{Re}\,\Phi_{ij}(t/x_1)\right]. \tag{27}$$

Again, using causality we can derive a Kramers-Kronig expression relating the two terms in the square brackets in Eq. (27). This allows us to eliminate the integral over s_1 and we arrive at the result

$$G_{ij}(x_1,t>0)=-\frac{1}{2\pi^2|x_1|}\frac{\partial}{\partial t}\,\mathrm{Re}\,\Phi_{ij}(t/x_1), \tag{28}$$

which has reduced the calculation of the point force response to a one-dimensional integral. For an anisotropic solid, numerical methods are in general required for the evaluation of the integral (26) and the method of integration has to cope with the Scholte wave, leaky RW and PSAW resonances, and the solid and liquid lateral waves.

C. Line and point focus acoustic images

In the acoustic microscopy experiments of Wolfe and co-workers,[18–20] the insonification is accomplished with an acoustic lens of finite aperture. The spatial Fourier transform of the force for normal insonification with a line focus lens of aperture angle θ is thus confined to the line segment $-s_0<s_1<s_0$, where $s_0=\sin\theta/v(\text{water})\approx 0.56\ \mu\text{s/mm}$ for $\theta=60°$, while for a point focus lens it is confined to a circular disk of the same radius and for an inclined point focus lens it is confined to a displaced elliptical region of similar dimensions. This has the effect of suppressing structures, such as the liquid lateral wave and Scholte wave, that propagate with slowness $s>s_0$.

In calculating the line force response normal to the surface, as measured by a pair of line focus lenses, Eq. (19) is modified by the removal of the portion of the integral in Eq. (17) over the intervals $[-\infty,-s_0]$ and $[s_0,\infty]$. We thus have that for $0<t<|x_1|s_0$

$$G_{33}(x_1,t)=-\frac{1}{\pi|x_1|}\,\mathrm{Im}\,\Psi_{33}(t/x_1,0)+f_{33}(x_1,t), \tag{29}$$

where

$$f_{33}(x_1,t)=\frac{1}{2\pi^2x_1}\left\{\int_{-\infty}^{-s_0}\frac{\mathrm{Re}\,\Psi_{33}(s_1,0)}{s_1-t/x_1}\right.$$
$$\left.+\int_{s_0}^{\infty}\frac{\mathrm{Re}\,\Psi_{33}(s_1,0)}{s_1-t/x_1}\right\}. \tag{30}$$

In considering a liquid-solid combination in which the liquid sound speed is considerably smaller than that of the solid, as is the case depicted in Fig. 1, $\mathrm{Re}\,\Psi_{33}(s_1,0)\approx 0$ in the region of s_0 and so $f_{33}(x_1,t)$ is a smooth function of t in the interval $[0,|x_1|s_0]$ and represents a small correction to $G_{33}(x_1,t)$. We have not included this correction in the calculated images presented later since our principal concern there is for the structures in these images and not the smoothly varying background.

For later times $t>|x_1|s_0$,

$$G_{33}(x_1,t)=\frac{-1}{2\pi^2x_1}\int_{-s_0}^{s_0}\frac{\mathrm{Re}\,\Psi_{33}(s_1,0)}{s_1-t/x_1}, \tag{31}$$

which is a continuous function of t, not revealing the liquid lateral wave and Scholte wave. In the limit of large t, $G_{33}(x_1,t)\sim 1/t$.

In calculating the point force response, as measured by a pair of point focus lenses, Eq. (26) is modified by cutting off the integral at $|\mathbf{s}_\parallel|=s_0$ rather than $\pm\infty$. All the structures that may be present in the images are captured in this way, but the liquid lateral wave and Scholte wave are suppressed.

The generation of a surface point force response image requires the evaluation of the line integral (26) and its differentiation with respect to t to obtain $G_{33}(\mathbf{x}_\parallel,t)$ for a 2D array of values of t and ϕ, the angle specifying the direction of the observation point in the surface. To minimize the number of function evaluations of $\Psi_{33}(\mathbf{s}_\parallel)$, in our coding we first calculate $\mathrm{Re}\,\Psi_{33}(\mathbf{s}_\parallel)$ for a 1200×1200 grid of values of $\mathbf{s}_\parallel$ and store these in a lookup table, which is subsequently consulted in calculating the line integrals. The entire process of calculating an image, examples of which are given later, takes in the region of 1 h on a 133-MHz Pentium personal computer.

The integration over s_2 in Eq. (26) is carried out along a line perpendicular to the viewing direction x_1, with $s_1=t/x_1$. As t is varied, there are certain times when the integration path is tangential to a threshold contour. At these instants, H_{33} displays nonanalytic behavior of some sort, e.g., a kink or discontinuity, which are the lateral waves in the point response. For the unloaded surface the resonance

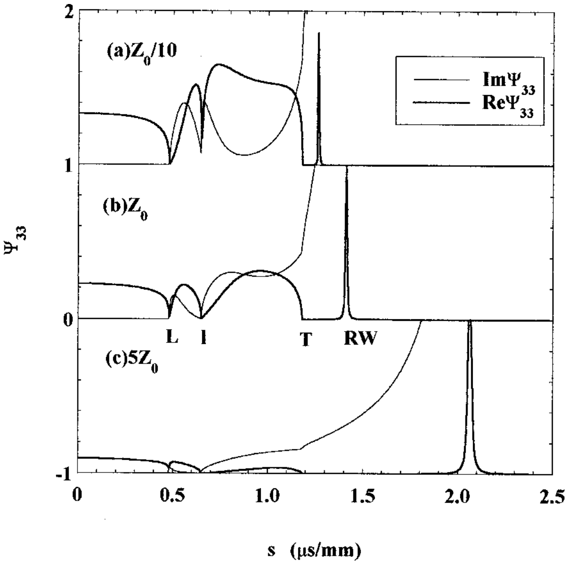

FIG. 3. Ψ_{33} for a slow solid, polyethylene, and the effects of varying the acoustic impedance of the loading liquid, ''water.'' (a) The impedance is one-tenth of that of water (shifted up), (b) the normal impedance of water; and (c) the impedance is five times that of water (shifted down). The negative portion of Im Ψ_{33} that occurs beyond RW is not shown.

associated with the leaky RW becomes infinitely sharp and, as a consequence, there are inverse square root surface wave arrival singularities conditioned on tangency of the integration path with the RW slowness curve. The bulk and RW arrivals propagate respectively at the bulk and surface wave group velocities in the direction x_1.

III. RESULTS FOR ISOTROPIC SOLIDS

A. Slow solids

There are quite a few solids, mainly organic, whose transverse wave speeds and in some cases even longitudinal wave speeds are less than the speed of sound in water. These solids span a range of densities and acoustic impedances. To explore the surface dynamical behavior of liquid-solid combinations in this category, we consider isotropic polyethylene, which has wave speeds $v(T)=0.85\ \mathrm{mm}/\mu\mathrm{s}$ and $v(L)=2.10\ \mathrm{mm}/\mu\mathrm{s}$ and density $\rho=1.37\ \mathrm{g/cm}^3$, in contact with a fluid that is nominally water, and examine what the effects of varying the acoustic impedance of the liquid, keeping the sound speed fixed, are. This variation is accomplished by changing the density and bulk modulus of the fluid by the same factor. The results are shown in Fig. 3.

Figure 3(a) depicts Ψ_{33} in the case where the impedance of the fluid has been reduced by a factor of 10 with respect to that of water. Due to the small influence of the fluid loading, the surface response is very similar to that for the free solid surface, having singular features at the lateral waves L and T and the RW. The main difference is the sharp narrow dip in Re Ψ_{33} and attendant swing in Im Ψ_{33} at $s(\text{water})$, which represents the fluid lateral wave l. The loading has in fact had the effect of increasing the RW slowness very slightly, from 1.252 μs/mm for the free surface to 1.263 μs/mm. The RW in this case represents a true interfacial wave lying in the subsonic region and consisting of partial wave components that fall off exponentially in both directions away from the surface. It is unattenuated as it travels along the surface and the broadening in Re Ψ_{33} that is apparent in this figure is purely the result of the artificial damping that has been introduced to render the surface wave visible.

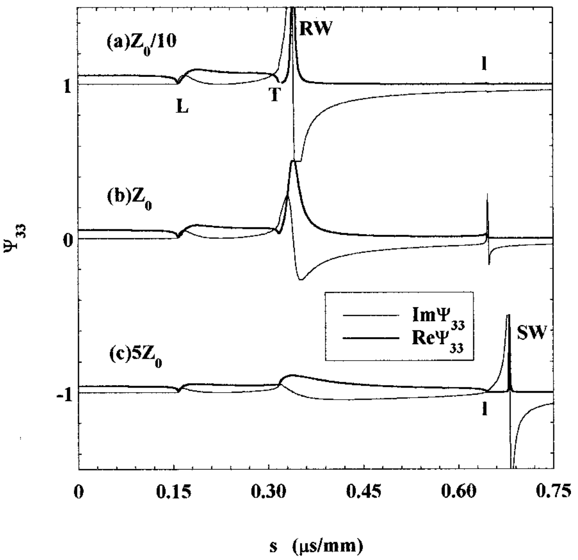

FIG. 4. Ψ_{33} for a fast solid, aluminum, and the effects of varying the acoustic impedance of the loading liquid, water. (a) The impedance is one-tenth of that of water (shifted up), (b) the normal impedance of water, and (c) the impedance is five times that of water (shifted down).

Figure 3(b) shows Ψ_{33} when the fluid impedance is equal to that of water. The lateral wave feature at l is now much more pronounced than before and the loading has had the effect of increasing the RW slowness to 1.413 μs/mm, which represents a 13% increase over that for the free surface.

Figure 3(c) shows the surface response when the fluid impedance is 5 times that of water. The interfacial wave slowness has increased to 2.07 μs/mm and the integrated value of Re Ψ_{33} for this wave relative to that for the bulk wave continuum is now much greater. With a further increase in the liquid impedance or, equivalently, a decrease in the solid impedance, the slowness of the interfacial wave continues to increase without limit. The kinetic energy of the wave resides more and more in the fluid and the potential energy in the solid. This is somewhat analogous to the situation for capillary waves on the surface of a liquid, but with the elastic restoring force of the solid performing the function of the surface tension.

B. Fast solids

The common metals, most covalent and ionic solids, and minerals have longitudinal and transverse wave speeds that exceed the speed of sound in water. To explore the surface dynamical behavior of liquid-solid combinations in this category, we consider isotropic aluminium, for which $v(T)=3.04\ \mathrm{mm}/\mu\mathrm{s}$ and $v(L)=6.42\ \mathrm{mm}/\mu\mathrm{s}$ and $\rho=2.7\ \mathrm{g/cm}^3$, in contact with a liquid that is nominally water, and examine what the effects of varying the acoustic impedance of the liquid, keeping the wave speed fixed, are. The results are shown in Fig. 4.

Figure 4(a) depicts Ψ_{33} in the case where the impedance of the fluid has been reduced by a factor of 10 with respect to that of water. Due to the small influence of the fluid loading, Ψ_{33} is similar to that for the free surface. There are, however, two important differences: The RW is now supersonic with respect to the sound speed in water and phase matching allows this wave to couple to bulk sound waves in the water, causing radiation of energy away from the surface. This results in the attenuation of this so-called leaky RW as it travels along the surface and endows the resonance in the response with a finite width. Beyond the RW slowness, Re Ψ_{33} falls off rapidly to a very small value, but approaching the sound slowness at l it increases slightly, drops to zero at l, and a little beyond this value displays a δ-function singularity of small integrated amplitude. This singularity lying in the fully subsonic region is associated with a true interfacial wave, the Scholte wave. In this limit it is essentially a bulk sound wave in the liquid, traveling parallel to the surface, which has become trapped at the surface and transformed into an interfacial wave by the finite compliance of the solid.

Figure 4(b) shows Ψ_{33} in the case where the fluid impedance is equal to that of water. The broadening and attenuation of the RW due to leakage into the water is now much greater. The increase in Re Ψ_{33} near l is is now more pronounced than before and the Scholte wave has a larger amplitude and separated a little further from the sound threshold.

Figure 4(c) shows Ψ_{33} when the fluid impedance is 5 times that of water. The RW is now barely recognizable as the broad feature that extends from T to l. The Scholte wave is now well separated from the continuum at $s = 0.680$ μs/mm. With a further increase in the liquid impedance, the slowness of the Scholte wave continues to increase and, just as in the previous case, this wave evolves into a capillarylike wave, with the solid elastic modulus providing the restoring force.

C. Solids ranging from fast to slow

To explore the different types of behavior that the wide range of relative fluid-solid velocities permits, we again consider the polyethylene-water combination and examine the effect of changing the sound speed (slowness) of the fluid while keeping the density constant. Figure 5(a) shows Ψ_{33} when the fluid slowness is 3 times that of water. The RW is supersonic with respect to the fluid and so is damped by leakage of energy into the fluid. The broadened resonance is centered at 1.247 μs/mm, slightly below the value for the unloaded surface. The fluid lateral wave and Scholte wave lie close to each other at approximately $3 \times s$ (water). For larger fluid slowness, the fluid lateral wave and Scholte wave diminish in size and approach each other as they increase in slowness.

Figure 5(b) shows Ψ_{33} when the fluid slowness is twice that of water. The RW is now very heavily damped and the Scholte wave is a more prominent feature, which moves down gradually as the fluid slowness is decreased, but remains above the RW slowness for the unloaded surface.

Figure 5(c) shows the surface response when the fluid is water. This is the same as Fig. 3(b). The Scholte wave has replaced the RW as the dominant surface mode and has taken on some of the character of the RW of the loaded surface.

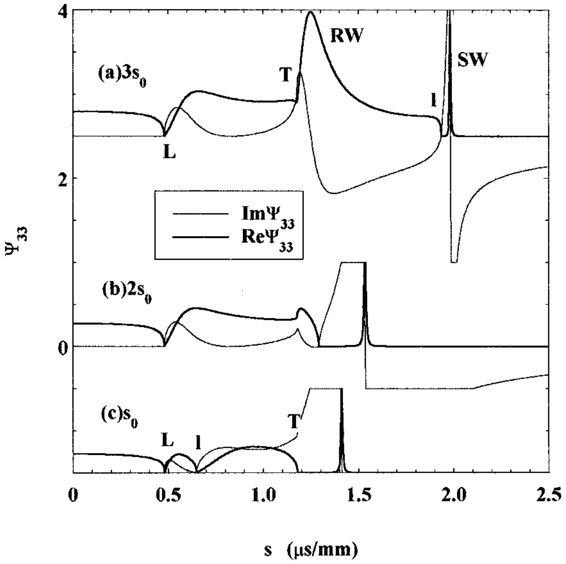

FIG. 5. Effects on Ψ_{33} of polyethylene, of varying the sound speed of the coupling fluid, water. (a) The fluid slowness is three times that of water (shifted up), (b) the fluid slowness is twice that of water, and (c) the normal slowness of water (shifted down).

Since there is scope for varying the properties of the coupling liquid in a continuous fashion, the effects described above are in many cases amenable to direct observation. Guzhev and Levin[10] have carried out an in-depth study of the effects of varying the fluid sound speed, taking $Bi_{12}GeO_{20}$ as their solid and an aqueous glycerol solution as coupling liquid. By altering the glycerol concentration, the sound speed in the solution can be varied from 1484 to 1913 m/s, which limits lie to either side of the RW speed 1680 m/s for the solid. Their measurements are in excellent accord with theory and show the Scholte wave tending to a value somewhat below the RW speed as the fluid speed increases.

IV. RESULTS FOR ANISOTROPIC SOLIDS

In this section we will discuss some of the solids that have been investigated experimentally by Vines and co-workers.[18–20,22] The first is a uniaxial carbon fiber epoxy composite that they have measured using line and point focus acoustic transducers.[20] The transverse velocity and density of this material are fairly close to that of the water transmission medium and as a result there is a complex interplay between the Scholte wave and the directionally dependent acoustic properties of the solid. Next we consider a number of cubic crystals whose densities and velocities are significantly greater than those of water.[19,22] For these, the Scholte wave is a very small feature in the surface response and shows little directional dependence. There is, however, striking anisotropy to be observed in the leaky RW and lateral waves of the solid. We discuss these effects for the principal crystal cuts of a number of crystals, of anisotropy coefficient $\eta = 2C_{44}/(C_{11} - C_{12})$ greater and less than unity.

A. Uniaxial carbon fiber epoxy composite

The solid consists of an array of fine carbon fibers aligned parallel to the sample surface and bonded together in an epoxy matrix. On a macroscopic scale this material behaves

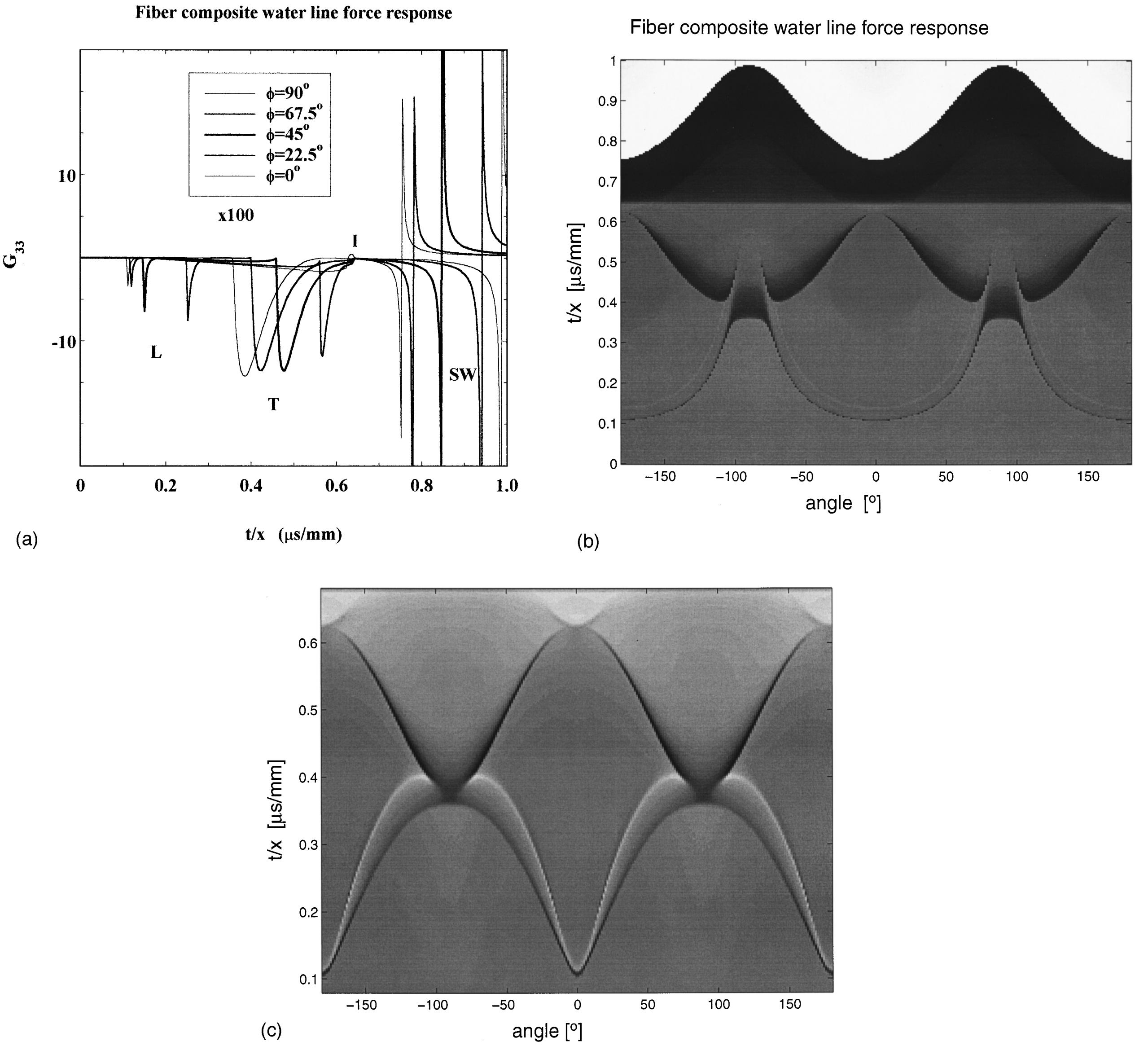

FIG. 6. Surface displacement response of uniaxial carbon fiber epoxy composite to impulsive forces. (a) Normal displacement response to a line force in five directions in the surface. Between 0 and 1 the response in magnified 100 times. ϕ is the angle between the fiber direction and the observation direction, which is perpendicular to the line along which the force is applied. (b) Directional dependence of the displacement response represented as a gray-scale image. The brighter regions correspond to positive displacement and the darker to negative displacement. To enhance the relatively small lateral wave features, the gray scale has been allowed to heavily saturate in the region of the Scholte wave, the sinusoidal-like feature near the top of the image. (c) Directional dependence of the point force response represented as a gray-scale image.

elastically as a transversely isotropic solid with effective elastic constants[20] $C_{11}=12.7$, $C_{12}=7.78$, $C_{13}=7.3$, $C_{33}=137$, $C_{44}=4.23$, and $C_{66}=2.46$ in GPa and density $\rho=1.65$ g/cm^3. Figure 6(a) shows the normal displacement response to impulsive line loading in five directions in the surface. The angle ϕ is between the fiber direction and the observation direction, which is perpendicular to the line along which the force is applied. The most conspicuous features are the longitudinal lateral wave of the solid L, the transverse lateral wave T, the water lateral wave l, and the Scholte wave SW. For clarity, the response between 0 and l has been magnified by 100. All except the water lateral wave are highly anisotropic. Figure 6(b) shows a gray-scale image generated by stacking together a large number of responses for a closely spaced set of directions in the surface. Brighter regions represent positive displacement and darker regions negative displacement. When the displacement becomes very large, the scale saturates towards white or black. The sharp structures in this image that lie below about $0.9\times s(\text{water}) \approx 0.6\ \mu$s/mm constitute the only ones that can be excited with the experimental arrangement of Wolfe and Vines[20] and this portion of the image is in good agreement with their measured line force image as regards the location of the lateral waves of the solid. In the measured image, preceding the lateral wave arrivals there is a smooth buildup of the signal corresponding to a displacement of opposite sign to that following the arrivals. This is indicative of a dipolar source function and is well reproduced by convoluting the calcu-

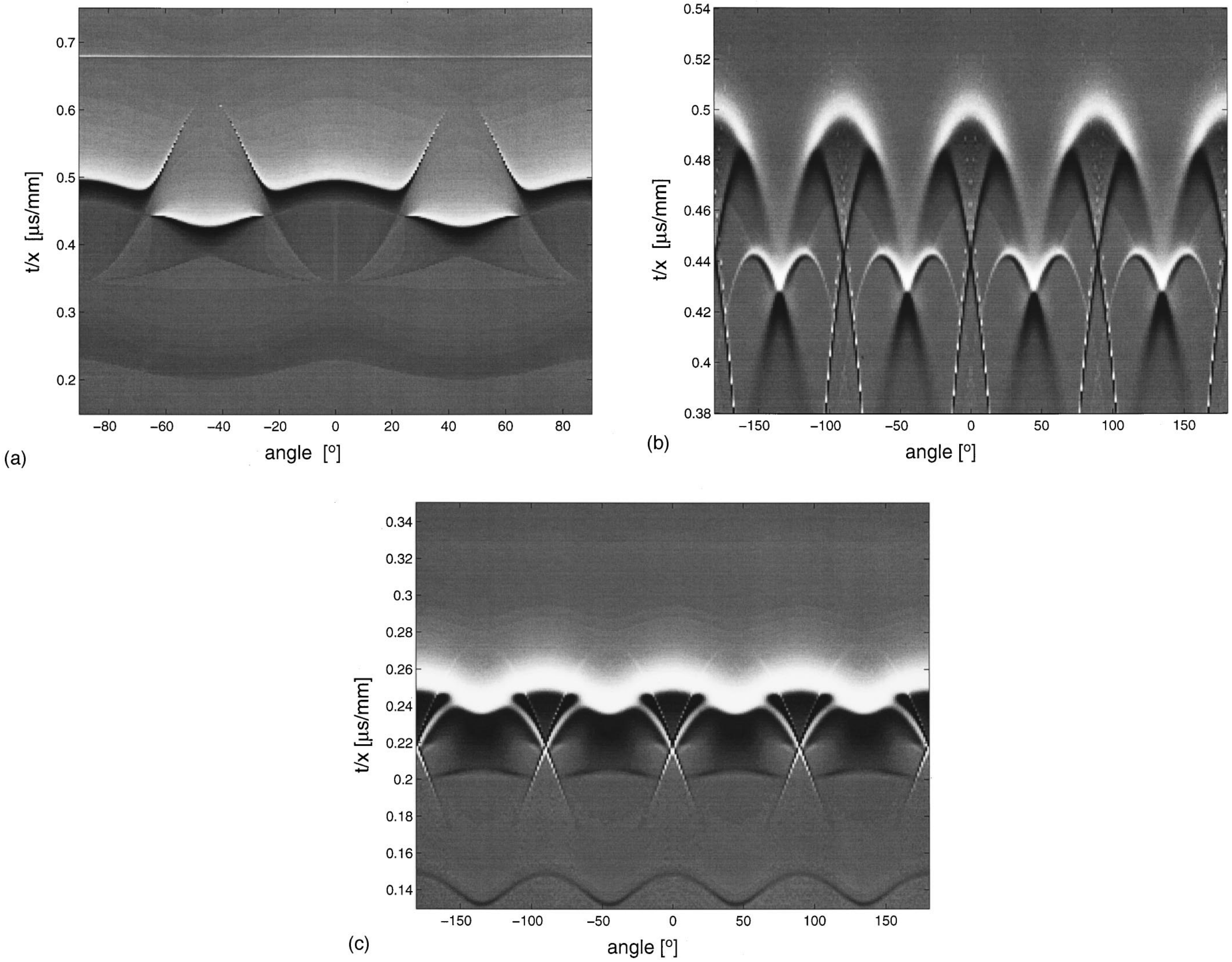

FIG. 7. (a) Line force response $G_{33}(\phi,t/l)$ for the water-loaded Cu(001) surface. (b) Point force response $G_{33}(\phi,t/l)$ for the water loaded Cu(001) surface. (c) Point force response $G_{33}(\phi,t/l)$ for the water loaded LiF(001) surface.

lated image with a source function of the type $F(t) = A\cos(2\pi f_0 t)\exp[-(t-t_c)^2/2\sigma^2]$, with $f_0 = 1$ MHz, $t_c = 0.375$ μs, and $\sigma = 0.375$ μs.

Figure 6(c) shows the calculated point force image for this fiber composite, restricted to the region below s(water), which is accessible to the acoustic microscopy measurements. While similarities can be seen between the line and point force images, there are also striking differences. In particular, the sharp structures in this case depict the directional dependence of the group slowness (inverse group velocity) $V^{-1}(\Theta_V)$ of the lateral waves, not their phase slowness. In the transformation from phase slowness to group slowness/velocity, points of inflection in the phase slowness curves map onto cusps in the group slowness curves. A set of four symmetry equivalent cusps in the fast transverse (FT) lateral wave at about 4 μs/mm is clearly in evidence. There is another set of four at about 2 μs/mm, but they are barely discernible because the displacements for these particular FT modes is almost parallel to the surface and so they contribute negligibly to the Green's function component G_{33}. They do, however, show up clearly in the case of G_{11} and G_{22}. Figure 6(c) is in good agreement with the measured point focus image.[20]

B. Cubic crystals of anisotropy $\eta > 1$

The existence of RW's and PSAW's and their variation with direction in the principal crystallographic cuts of cubic crystals have been surveyed by Farnell[31] and by Every.[32] The latter report also describes the threshold bulk wave curves, which are the lateral waves of the fluid loaded surface.

Figure 7(a) is a gray-scale representation of the line force response $G_{33}(\phi,t/l)$ for the water loaded Cu(001) surface. Copper is a crystal characterized by a large anisotropy $\eta = 3.204$, large density compared to water $\rho = 8.96$ g/cm^3, and RW and PSAW slownesses that, although smaller than s(water) in all directions, approach within 20% of the latter slowness in the $\langle 110 \rangle$ directions. In the vicinity of the $\langle 100 \rangle$ directions the most prominent feature is the damped leaky RW, of slowness ~ 0.48 μs/mm. The RW slowness is highly anisotropic and away from the $\langle 100 \rangle$ directions it diminishes in intensity in the image as the polarization of this mode tilts over to the horizontal, vanishing in the $\langle 110 \rangle$ directions where the RW degenerates with the ST bulk mode. In the region of the $\langle 110 \rangle$ directions the most prominent feature is the PSAW, with a slowness of ~ 0.43 μs/mm, which is

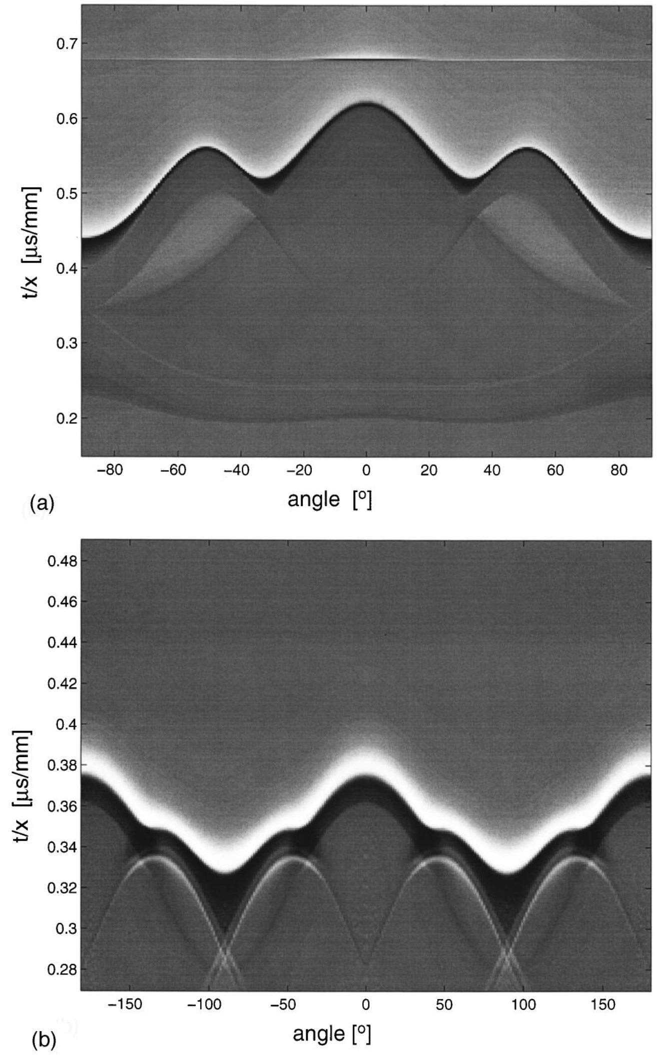

FIG. 8. (a) Line force response $G_{33}(\phi,t/l)$ for the water-loaded Cu(110) surface. (b) Point force response $G_{33}(\phi,t/l)$ for the water-loaded Ge(110) surface.

damped by leakage of energy into the water and away from the ⟨110⟩ directions, also through coupling to bulk modes in the solid. In the region midway between the ⟨100⟩ and ⟨110⟩ directions the RW and PSAW have comparable intensities. The lateral waves of the copper are revealed as a set of sharp lines (other than the RW and PSAW) where there is a sudden change in the intensity. The structures in the region extending from $\sim$0.34 to $\sim$0.62 μs/mm are the transverse lateral waves and the sinusoidal-like structure between 0.20 and 0.23 μs/mm is the longitudinal lateral wave. The disposition of these various structures is consistent with the pattern of surface and threshold bulk waves described in Ref. 32. The Scholte wave is the almost straight line at 0.677 μs/mm, which shows an almost imperceptible variation of slowness/velocity with direction and only slight splitting from the water lateral wave, but a noticeable variation of intensity. Because the water slowness does not greatly exceed the ST slowness of the solid, this wave is a fairly prominent feature in this image.

Figure 7(b) shows an image representing the calculated point force response $G_{33}(\phi,t/l)$ for the water-loaded Cu(001) surface. The most prominent structures in this image are again the leaky RW and PSAW. The upper set of bright arches and their darker V-shaped supports belong to the RW. Their junction is a cusp in the group slowness curve, which maps from a point of inflection in the phase slowness curve. The lower set of bright M-shaped arches is associated with the PSAW. There are fainter features associated with the lateral waves. This image, with its complexity and striking detail, is in good agreement with the Cu(001) point focus image measured by Vines, Hauser, and Wolfe.[19]

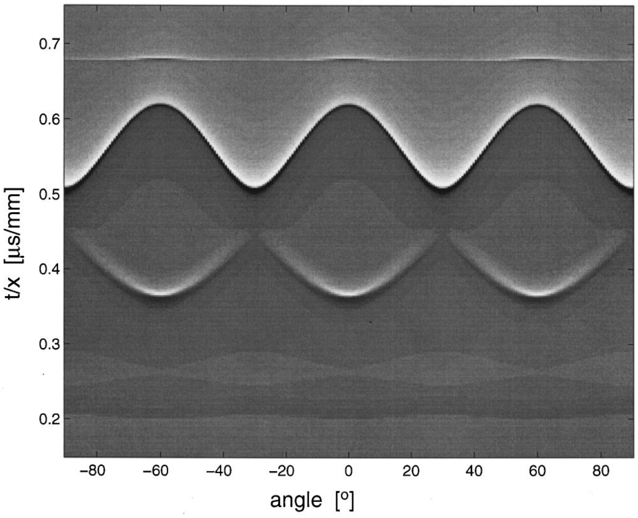

FIG. 9. Line force response $G_{33}(\phi,t/l)$ for the water-loaded Cu(111) surface.

Figure 7(c) shows the calculated $G_{33}(\phi,t/l)$ point force image for the water-loaded LiF(001) surface, for which $\rho = 2.601$ g/cm^3 and $\eta = 1.815$, both of which are significantly smaller than for Cu. The water loading causes considerable broadening of the RW and PSAW, with the result that in the image they appear as the connected undulating bright structure. The rounded legs protruding below are part of the PSAW structure. The sharp arches cutting through the RW band are the ST lateral wave. The slightly undulating struc-

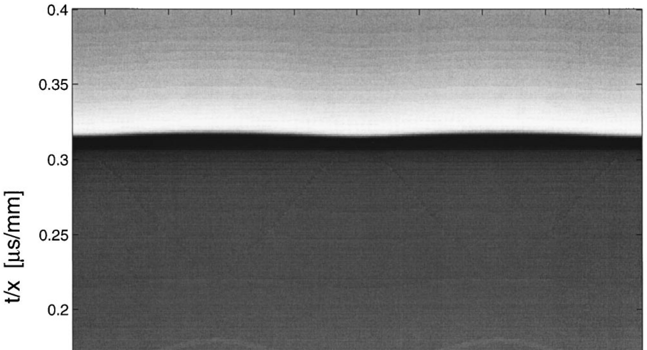

FIG. 10. Line force response $G_{33}(\phi,t/l)$ for the water-loaded CaF(001) surface.

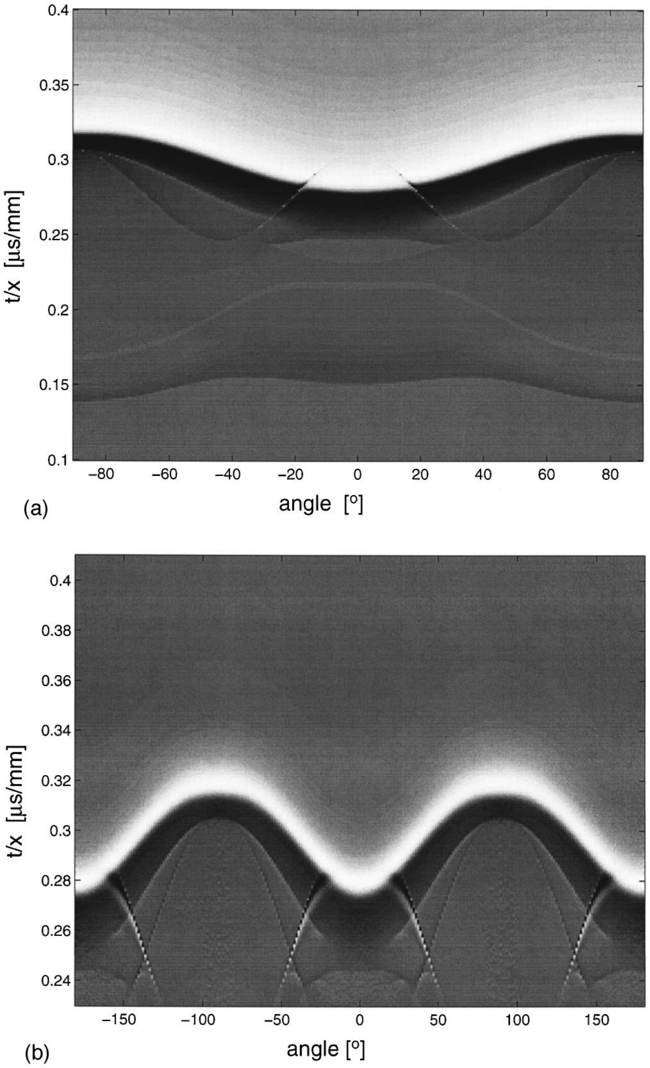

FIG. 11. (a) Line force response $G_{33}(\phi,t/l)$ for the water-loaded CaF(110) surface. (b) Point force response $G_{33}(\phi,t/l)$ for the water-loaded CaF(110) surface.

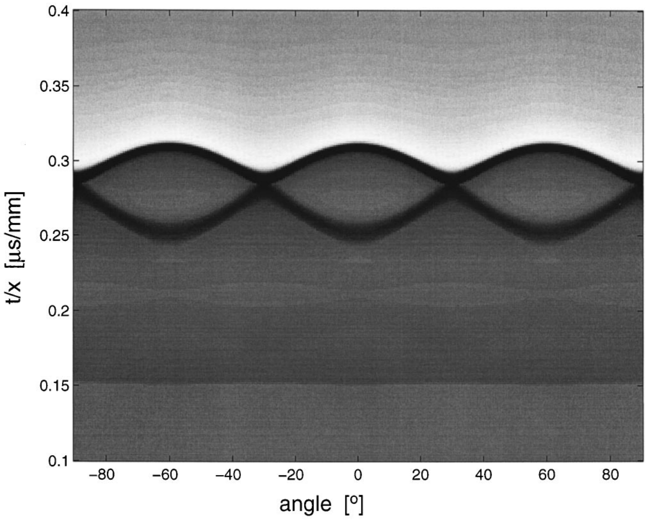

FIG. 12. Line force response $G_{33}(\phi,t/l)$ for the water-loaded CaF(111) surface.

ture at ~ 0.2 μs/mm is the FT lateral wave and the more prominent undulating structure between ~ 0.13 and ~ 0.15 μs/mm is the L lateral wave. This image is in good with the measurement.[19]

Figure 8(a) shows the calculated $G_{33}(\phi,t/l)$ line force response for the water-loaded Cu(110) surface. The most prominent structure in this image is the leaky RW. The transverse lateral waves are fairly faint structures, but in the corresponding images of $G_{11}(\phi,t/l)$ and $G_{22}(\phi,t/l)$ they show up as very sharp intense features. The L lateral wave lies just above 0.2 μs/mm. These structures are consistent with Fig. 12 of Ref. 32. As in the case of Cu(001), the Scholte wave and water lateral wave cannot be resolved and show negligible variation in slowness with direction, but significant intensity variation with direction.

Figure 8(b) shows the calculated $G_{33}(\phi,t/l)$ point force image of the water-loaded Ge(110) surface ($\rho = 5.322$ g/cm^3 and $\eta = 1.665$). In appearance the structure for the leaky RW is similar to that for the line force image of this surface. The sharp split arched structures underneath are transverse lateral waves. This image is in good agreement with the point focus image of Ge(110) measured by Vines, Hauser, and Wolfe.[19]

Figure 9 shows the calculated $G_{33}(\phi,t/l)$ line force image for the water-loaded Cu(111) surface. Because $\langle 111 \rangle$ is an axis of six-fold rotational inversional symmetry for the medium, the images displays six-fold rotational symmetry. The most prominent feature is the leaky RW and the somewhat less intense matching inverted structure originates in a resonance near to the FT lateral wave. There is the fainter L lateral wave near 0.2 μs/mm. These are all consistent with Fig. 14 of Ref. 32. As in the other two surface orientations of Cu, the Scholte wave and water lateral wave cannot be resolved and show negligible variation in slowness with direction, but significant intensity variation with direction.

C. Cubic crystals of anisotropy $\eta < 1$

The results presented in this section are illustrative of the case of anisotropy $\eta < 1$. Figure 10 shows the calculated $G_{33}(\phi,t/l)$ line force image for the water-loaded CaF(001) surface ($\rho = 3.18$ g/cm^3 and $\eta = 0.575$). For this high-velocity crystal, all the surface and lateral wave structures lie at slownesses well below s(water). The water lateral wave and Scholte wave are consequently extremely faint features separated only very slightly from each other. This and the other images for CaF are thus restricted the slowness range of the RW and solid lateral waves. For crystals with $\eta < 1$, the ST lateral wave for the (001) surface is the pure T mode, polarized normal to the (001) surface, and its slowness is $\sqrt{\rho / C_{44}}$, independent of direction. This has the result that the RW varies hardly at all with direction and there is no PSAW. The L lateral wave shows more variation with direction, around a mean value of approximately 0.15 μs/mm.

Figure 11(a) shows the calculated $G_{33}(\phi,t/l)$ line force image for the water-loaded CaF(110) surface. The prominent broad structure is, within $\sim 20°$ of $\phi = 0$, a PSAW, while elsewhere it is a leaky RW. All the sharp structures in the image are lateral waves and are consistent with Fig. 20 of Ref. 32. Figure 11(b) shows the corresponding point force image. Here too the leaky RW and PSAW form an almost continuous band, only broken partly by the ST lateral wave that separates the RW and PSAW in the line force image. The other sharp features in Fig. 11(a) are lateral waves. These map onto corresponding features in the line force image. Figure 11(b) is in good agreement with the measured point focus image of CaF(110).

Figure 12 shows the calculated $G_{33}(\phi,t/l)$ line force image for the water-loaded CaF(111) surface. It bears some resemblance to the Cu(111) image. The most prominent structure is due to the leaky RW and there is a similar but less intense inverted structure that is a resonance that follows the angular variation of the FT lateral wave slowness (see Fig. 22 of Ref. 32).

V. CONCLUSIONS

In conclusion, we have presented algorithms for calculating the 2D and 3D dynamic Green's functions of a pair of joined anisotropic elastic half spaces. We have used them to calculate the normal surface responses of fluid-loaded isotropic and anisotropic solids to impulsive line and point forces. The responses show prominent features associated with the Scholte interfacial wave, leaky Rayleigh and pseudosurface acoustic waves, and lateral waves of the solid and liquid, i.e., surface skimming bulk waves of the two media. Images representing the directional and time dependence of the line and point force responses are in good agreement with corresponding acoustic microscopy images measured by Vines and co-workers in a number of anisotropic solids using a pair of line or point focus lenses. Because of the finite aperture of the lenses, structures lying close to and beyond the water lateral wave in slowness are not coupled to and are absent from the measured images. This effect is simulated by introducing a finite cutoff in the Fourier transform of the forcing function. Other methods of excitation and detection exist that would allow these late arriving features to be observed. The analytic methods described in this paper can be expected to find application in diverse areas such as materials characterization and nondestructure testing, physical acoustics, and seismology.

ACKNOWLEDGMENTS

A.G.E. would like to thank P. Zinin, A. A. Maznev, and S. Tamura for valuable discussions. R. E. Vines and J. P. Wolfe are thanked for allowing us access to their unpublished results. The hospitality of the Department of Materials at Oxford University is greatly appreciated. Financial support has been provided by the University of the Witwatersrand, The South African Foundation for Research Development, and the Oppenheimer Fund.

---

[1] B. A. Auld, *Acoustic Fields and Waves in Solids* (Wiley, New York, 1973).

[2] J. D. Achenbach, *Wave Propagation in Elastic Solids* (North-Holland, Amsterdam, 1973).

[3] L. M. Brekhovsikh and O. A. Godin, *Acoustics of Layered Media I* (Springer-Verlag, Berlin, 1990).

[4] A. N. Nayfeh, *Wave Propagation in Layered Anisotropic Media* (North-Holland, Amsterdam, 1995).

[5] H. L. Bertoni and T. Tamir, Appl. Phys. **2**, 157 (1973).

[6] H. Uberall, in *Physical Acoustics*, edited by W. P. Mason and R. N. Thurston (Academic, New York, 1973), Vol. X, p. 1.

[7] R. H. Tew, Proc. R. Soc. London, Ser. A **437**, 433 (1992).

[8] M. de Billy and G. Quentin, J. Appl. Phys. **54**, 4314 (1983).

[9] V. Gusev, C. Desmet, W. Lauriks, G. Glorieux, and J. Thoen, J. Acoust. Soc. Am. **100**, 1514 (1996); C. Desmet, V. Gusev, W. Lauriks, C. Glorieux, and J. Thoen, Appl. Phys. Lett. **68**, 2939 (1996).

[10] S. N. Guzhev, J. Acoust. Soc. Am. **95**, 661 (1994); S. N. Guzhev and V. M. Levin, Sov. Phys. Acoust. **33**, 355 (1987).

[11] S. Nasr, J. Duclos, and M. Leduc, J. Acoust. Soc. Am. **87**, 507 (1990).

[12] Y. Tsukahara, Y. Liu, C. Neron, C. K. Jen, and J. Kushibiki, IEEE Trans. Ultrason. Ferroelectr. Freq. Control **41**, 458 (1994).

[13] J. P. Sessarego, J. Sageloli, C. Gazanhes, and H. Uberall, J. Acoust. Soc. Am. **101**, 135 (1997).

[14] A. N. Norris and B. K. Sinha, J. Acoust. Soc. Am. **98**, 1147 (1995).

[15] N. Favretto-Anres, Acust. Acta Acust. **82**, 829 (1996).

[16] A. Briggs, *Acoustic Microscopy* (Clarendon, Oxford, 1992).

[17] A. G. Every, A. A. Maznev, and G. A. D. Briggs, Phys Rev. Lett. **79**, 2478 (1997).

[18] R. E. Vines, S. Tamura, and J. P. Wolfe, Phys. Rev. Lett. **74**, 2729 (1995).

[19] R. E. Vines, M. R. Hauser, and J. P. Wolfe, Z. Phys. B **98**, 255 (1995).

[20] J. P. Wolfe and R. E. Vines, Proc. IEEE Ultrasonics Symposium **96**, 607 (1996).

[21] S. Tamura, R. E. Vines, and J. P. Wolfe, Phys. Rev. B **54**, 5151 (1996).

[22] A. Ikehata, R. E. Vines, S. Tamura, and J. P. Wolfe, Physica B **219&220**, 710 (1996).

[23] N. N. Hsu, D. Xiang, S. E. Fick, and G. V. Blessing, Proc. IEEE Ultrasonics Symposium **95**, 867 (1995).

[24] W. Li and J. D. Achenbach, IEEE Trans. Ultrason. Ferroelectr. Freq. Control **44**, 681 (1997).

[25] M. G. Somekh, G. A. D. Briggs, and C. Ilett, Philos. Mag. A **49**, 179 (1984).

[26] J. Kushibiki, K. Horii, and N. Chubachi, Electron. Lett. **19**, 404 (1983).

[27] A. A. Maznev and A. G. Every, Int. J. Eng. Sci. **35**, 321 (1997).

[28] A. G. Every, K. Y. Kim, and A. A. Maznev, J. Acoust. Soc. Am. **102**, 1346 (1997).

[29] R. Stoneley, Proc. R. Soc. London, Ser. A **106**, 416 (1924).

[30] D. M. Barnett, J. Lothe, S. D. Gavazza, and M. J. P. Musgrave, Proc. R. Soc. London, Ser. A **402**, 153 (1985).

[31] G. W. Farnell, in *Physical Acoustics*, edited by W. P. Mason and R. N. Thurston (Academic, New York, 1970), Vol. VI, p. 109.

[32] A. G. Every, Phys. Rev. B **33**, 2719 (1986).